

# Annotation-efficient cancer detection with report-guided lesion annotation for deep learning-based prostate cancer detection in bpMRI

Joeran Bosma<sup>a,\*</sup>, Anindo Saha<sup>1,a</sup>, Matin Hosseinzadeh<sup>1,a</sup>, Ilse Slootweg<sup>1,a</sup>, Maarten de Rooij<sup>1,a</sup>, Henkjan Huisman<sup>1,a</sup>

<sup>a</sup>*Diagnostic Image Analysis Group, Radboud University Medical Center, Nijmegen 6525 GA, The Netherlands*

## ARTICLE INFO

*Article history:*

*Keywords:* Annotation efficiency, computer-aided detection and diagnosis, magnetic resonance imaging, prostate cancer, semi-supervised deep learning.

## ABSTRACT

Deep learning-based diagnostic performance increases with more annotated data, but large-scale manual annotations are expensive and labour-intensive. Experts evaluate diagnostic images during clinical routine, and write their findings in reports. Leveraging unlabelled exams paired with clinical reports could overcome the manual labelling bottleneck. We hypothesise that detection models can be trained semi-supervised with automatic annotations generated using model predictions, guided by sparse information from clinical reports. To demonstrate efficacy, we train clinically significant prostate cancer (csPCa) segmentation models, where automatic annotations are guided by the number of clinically significant findings in the radiology reports. We included 7,756 prostate MRI examinations, of which 3,050 were manually annotated. We evaluated prostate cancer detection performance on 300 exams from an external centre with histopathology-confirmed ground truth. Semi-supervised training improved case-based diagnostic area under the receiver operating characteristic curve (AUROC) from  $87.2 \pm 0.8\%$  to  $89.4 \pm 1.0\%$  ( $P < 10^{-4}$ ) and improved lesion-based sensitivity at one false positive per case from  $76.4 \pm 3.8\%$  to  $83.6 \pm 2.3\%$  ( $P < 10^{-4}$ ). Semi-supervised training was  $14.4\times$  more annotation-efficient for case-based performance and  $5.7\times$  more annotation-efficient for lesion-based performance. This improved performance demonstrates the feasibility of our training procedure. Source code is publicly available at [github.com/DIAGNijmegen/Report-Guided-Annotation](https://github.com/DIAGNijmegen/Report-Guided-Annotation). Best csPCa detection algorithm is available at [grand-challenge.org/algorithms/bpmri-cspca-detection-report-guided-annotations/](https://grand-challenge.org/algorithms/bpmri-cspca-detection-report-guided-annotations/).

© 2022

## 1. Introduction

Computer-aided diagnosis (CAD) systems in fields where clinical experts are matched or outperformed, typically use very large training datasets. Top performing deep learning systems used 29,541 training cases (10,306 patients) for the detection of lung cancer (Ardila et al., 2019), 121,850 training cases (121,850 women) for the detection of breast cancer (McKinney et al., 2020) and 16,114 training cases (12,399 patients) for the classification of skin diseases (Liu et al., 2020).

Annotation time and cost are major limiting factors, resulting in significantly smaller labelled training datasets in most deep learning fields. In the natural image domain, leveraging sam-

ples without target task annotations has proven to be effective, even when manually labelled samples are abundant. On ImageNet, with 1.3 million manually labelled training samples, all ten leaderboard holders of the past four years used additional training samples with automatically generated labels. Several approaches were used: (Mahajan et al., 2018) used 3.5 billion images from Instagram to pre-train their models by predicting the corresponding hashtag (*transfer learning*); (Xie et al., 2020) used a *teacher* model to predict 300 million images scraped from the web and selected 130 million samples to train a new *student* model (*self-training*); and (Pham et al., 2021) pushed the teacher-student approach further by continuously updating the teacher model with reinforcement learning. Although the other seven leaderboard holders primarily pursued different research directions, they did incorporate automatic labelling techniques to reach state-of-the-art performance.

\*Corresponding author:  
e-mail: Joeran.Bosma@radboudumc.nl (Joeran Bosma)

In the medical domain, popular techniques to leverage unlabelled samples include transfer learning from a distant or related task, and self-training with automatically generated labels (Cheplygina *et al.*, 2019). Other techniques to leverage unlabelled samples include contrastive learning (Chaitanya *et al.*, 2020; Sowrirajan *et al.*, 2021; Azizi *et al.*, 2021) and self-supervised representation learning (Zhou *et al.*, 2019). These techniques either pre-train without labels, or directly use model predictions as true labels.

Leveraging clinical information, which is often available in medical reports, to improve training with unlabelled samples is under-explored. Clinical information from reports typically differ from regular training annotations, but can inform the generation of automatic annotations for self-training. One study, (Bulten *et al.*, 2019), generated pixel-level Gleason score annotations in H&E stained prostate biopsies by leveraging pathology reports. First, they generated precise cancer masks. Then, they extracted the Gleason scores from the pathology reports to classify the cancer masks into Gleason grades. These steps allowed the generation of Gleason score annotations in thousands of prostate biopsies, which would have been infeasible to obtain manually. Incorporating clinical information to guide automatic annotations for self-training remains to be investigated for medical tasks other than biopsy grading.

We hypothesise that medical detection tasks, where the structures of interest can be counted, can leverage unlabelled cases by semi-supervised training with report-guided annotations. Specifically, we focus on lesion detection, where each case can have any number of lesions. To demonstrate feasibility of our method, we developed a semi-supervised training procedure for clinically significant prostate cancer detection in MRI.

Prostate cancer (PCa) has 1.2 million new cases each year (Sung *et al.*, 2021), a high incidence-to-mortality ratio and risks associated with treatment and biopsy; making non-invasive diagnosis of clinically significant prostate cancer (csPCa) crucial to reduce both overtreatment and unnecessary (confirmatory) biopsies (Stavriniades *et al.*, 2019). Multiparametric MRI (mpMRI) scans interpreted by expert prostate radiologists provide the best non-invasive diagnosis (Eldred-Evans *et al.*, 2021), but is a limited resource that cannot be leveraged freely. Computer-aided diagnosis (CAD) can assist radiologists to diagnose csPCa, but present-day solutions lack stand-alone performance comparable to that of expert radiologists (Cao *et al.*, 2021; Saha *et al.*, 2021; Hosseinzadeh *et al.*, 2021; Schelb *et al.*, 2019; Seetharaman *et al.*, 2021).

Datasets used for prostate cancer detection and diagnosis have significantly fewer training samples than datasets used to train top-performing deep learning systems in other medical fields (Ardila *et al.*, 2019; McKinney *et al.*, 2020; Liu *et al.*, 2020). Studies tackling csPCa detection in MRI by training on histopathology-confirmed annotations, used datasets with 66-806 (median: 146) samples to train their deep learning system (Schelb *et al.*, 2019; Arif *et al.*, 2020; Sanyal *et al.*, 2020; Aldoj *et al.*, 2020; Bhattacharya *et al.*, 2020; Cao *et al.*, 2019; Seetharaman *et al.*, 2021; Netzer *et al.*, 2021). Approaches using radiologically-estimated annotations (reported using Prostate Imaging Reporting and Data System: Version 2

(PI-RADS)) used 687-1,736 (median: 1,584) training samples (Sanford *et al.*, 2020; Yu *et al.*, 2020b,a; Saha *et al.*, 2021; Hosseinzadeh *et al.*, 2021).

Prior work investigated the effect of training set size on prostate cancer detection performance, with radiologically-estimated ground truth for training and testing (Hosseinzadeh *et al.*, 2021). This work shows patient-based area under the receiver operating characteristic curve (AUROC) for their internal test set increased logarithmically between 50 and 1,586 training cases, from an AUROC of 79.9% to 87.5%. If this trend continues, tens of thousands of annotated cases would be required to reach expert performance — in concordance with similar applications in medical imaging.

Trained investigators supervised by an experienced radiologist annotated all PI-RADS  $\geq 4$  findings in more than three thousand of our institutional prostate MRI exams. According to our principal annotator, I.S., she requires about four minutes to annotate a single prostate cancer lesion in 3D. Difficult cases are discussed with radiologists, further increasing the overall duration. Annotating tens of thousands of cases would therefore incur huge costs and an incredibly large time investment.

Our report-guided semi-supervised training procedure aims to leverage unlabelled exams paired with clinical reports, to improve detection performance without any additional manual effort. We investigate the efficacy of our training procedure by comparing semi-supervised training of csPCa detection models against supervised training. First, we investigate the setting with 3,050 manually annotated exams and 4,706 unlabelled exams. Secondly, we investigate several labelling budgets: 100, 300, 1,000 or 3,050 manually annotated exams, paired with the remaining 7,656, 7,456, 6,756 or 4,706 unlabelled exams, respectively. Finally, to determine annotation-efficiency, we compare supervised training performance with 3,050 manually annotated exams against semi-supervised training with reduced manual annotation budgets.

In this study, the training procedure with report-guided automatic annotations is presented for csPCa detection in bpMRI using radiology reports. However, the underlying method is neither limited to csPCa, MRI, nor radiology reports, and can be applied universally. Any detection task with countable structures of interest, and clinical information reflecting these findings, can use our training method to leverage unlabelled exams with clinical reports.

## 2. Materials and Methods

### 2.1. Datasets

Two datasets with biparametric MRI (bpMRI) scans (axial T2-weighted (T2W), high b-value ( $\geq 1400$ ) diffusion-weighted imaging (DWI) and apparent diffusion coefficient (ADC) maps) for prostate cancer detection were used.

To train and tune our models, 7,756 studies (6,380 patients) out of 9,275 consecutive studies (7,430 patients) from Radboud University Medical Centre (RUMC) were included. 1,519 studies were excluded due to incomplete examinations, preprocessing errors, prior treatment, poor scan quality, or a prior positive biopsy (Gleason grade group  $\geq 2$ ). All scans were obtained as

part of clinical routine and evaluated by at least one of six experienced radiologists (4–25 years of experience with prostate MRI). All 1,315 csPCa lesions (PI-RADS  $\geq 4$ ) in 3,050 studies between January 2016 and August 2018 were manually delineated by trained investigators (at least 1 year of experience), supervised by an experienced radiologist (M.R., 7 years of experience with prostate MRI).

To test our models, an external dataset of 300 exams (300 patients) from Ziekenhuisgroep Twente (ZGT) was used, acquired between March 2015 and January 2017. All patients in the test set received TRUS biopsies and patients with suspicious findings on MR also received MR-guided biopsies. For 61 exams (20.3%) the ground truth was derived from radical prostatectomy, which superseded the biopsy findings. All examinations in the test set have histopathology-confirmed ground truth, while retaining the patient cohort observed in clinical practice.

Further details on patient demographics, study inclusion/exclusion criteria and acquisition parameters can be found in the Supplementary Materials.

## 2.2. Report-guided Automatic Annotation

Radiology reports were used to automatically create voxel-level annotations for csPCa. At a high level, our labelling procedure consists of two steps:

1. Count the number of clinically significant findings in each radiology report,
2. Localise these findings in their corresponding bpMRI scans with a prostate cancer segmentation model.

A rule-based natural language processing script was developed to automatically extract the PI-RADS scores from radiology reports. The number of clinically significant findings,  $n_{\text{sig}}$ , is then defined as the number of PI-RADS  $\geq 4$  findings in an exam. The clinically significant findings are localised by keeping the  $n_{\text{sig}}$  most confident candidates from a csPCa segmentation model, as depicted in Figure 1. These automatically generated voxel-level masks can be used to augment the training dataset and produce new csPCa segmentation models.

### 2.2.1. Extraction of Report Findings

Most of the radiology reports in our dataset were generated from a template, and modified to provide additional information. Although multiple templates were used over the years, this resulted in structured reports for most exams. This makes a rule-based natural language processing script a reliable and transparent way to extract PI-RADS scores from our radiology reports.

Simply counting the occurrences of ‘PI-RADS 4/5’ in the report body is reasonably effective, but has some pitfalls. For example, prior PI-RADS scores are often referenced during follow-up exams, resulting in false positive matches. Findings can also be grouped and described jointly, resulting in false negatives. To improve the reliability of the PI-RADS extraction from radiology reports, we extracted the scores in two steps.

First, we tried to split the radiology reports in sections for individual findings. Secondly, we extracted the PI-RADS scores

for each section individually. In case the report could not be split in sections per lesion, we applied strict pattern matching on the full report. See the Supplementary Materials for more details. Example report sections are shown in Figure 2.

### 2.2.2. Localisation of Report Findings

To localise csPCa findings in unlabelled bpMRI scans, we employed an ensemble<sup>1</sup> of csPCa segmentation models. From the resulting voxel-level confidence maps we created distinct lesion candidates, as illustrated in Figure 3. Specifically, we created a lesion candidate by starting at the most confident voxel, and including all connected voxels (in 3D) with at least 40% of the peak’s confidence. Then, the candidate lesion is removed from the confidence map, and the process is repeated until no candidates remain or a maximum of 5 lesions are extracted. Tiny candidates of 10 or fewer voxels ( $\leq 0.009 \text{ cm}^3$ ) are discarded.

Automatic voxel-level csPCa annotations were generated by keeping the  $n_{\text{sig}}$  most confident lesion candidates, with  $n_{\text{sig}}$  the number of clinically significant report findings as described in Section 2.2.1. If there were fewer lesion candidates than clinically significant report findings, the automatic label is excluded.

## 2.3. Models, Preprocessing and Data Augmentation

We have posed the prostate cancer detection task as a voxel-level segmentation task and employed two independent architectures, *nnU-Net* and Dual-Attention U-Net (*DA-UNet*). *nnU-Net* is a self-configuring framework that follows a set of rules to select the appropriate architecture based on the input dataset (Isensee *et al.*, 2021). The *DA-UNet* architecture was developed specifically for csPCa detection, where it performed best among state-of-the-art architectures (Saha *et al.*, 2021). Both are derived from the *U-Net* architecture (Ronneberger *et al.*, 2015), extended to 3D (Çiçek *et al.*, 2016), and use anisotropic pooling or convolutional strides to account for the difference in through-plane and in-plane resolution of prostate MRI. See the Supplementary Materials for more details.

The *nnU-Net* framework typically uses the sum of cross-entropy and soft Dice loss, and applies the loss at multiple resolutions (deep supervision). Motivated by Baumgartner *et al.* (2021) and exploratory experiments, we trained *nnU-Net* using cross-entropy only. Based on prior experience (Saha *et al.*, 2021), we trained the *DA-UNet* model with Focal Loss ( $\alpha = 0.75$ ) (Lin *et al.*, 2017).

The acquisition protocol of bpMRI ensures negligible movement between imaging sequences, and little deviation of the prostate from the centre of the scan. Therefore, neither registration between sequences, nor centring of the prostate was deemed necessary. In previous work, we have observed that a centre crop size of  $72.0 \text{ mm} \times 72.0 \text{ mm} \times 64.8 \text{ mm}$  at a resampled resolution of  $0.5 \text{ mm} \times 0.5 \text{ mm} \times 3.6 \text{ mm/voxel}$  works well for our dataset (Saha *et al.*, 2021). To prevent the *nnU-Net*

<sup>1</sup>Multiple models were ensembled by averaging the softmax confidence maps, which resulted in more consistent segmentation masks compared to a single model. The ensemble also improved localisation of report findings in difficult cases, where a single model was more likely to miss the lesion.

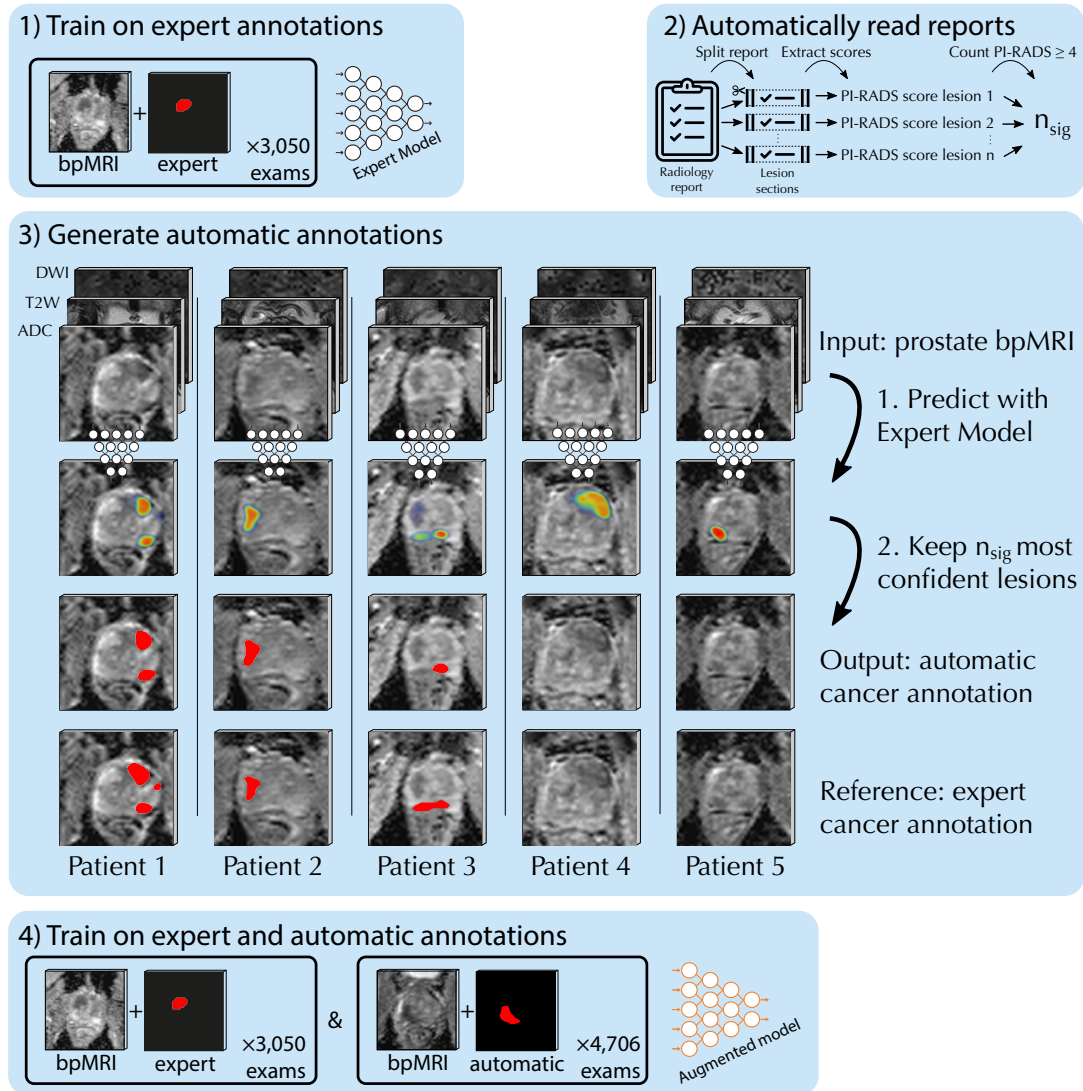


**Fig. 1.** Overview of the steps to create automatic annotations for the unlabelled RUMC exams. 1) Train a prostate cancer segmentation model on manually annotated clinically significant prostate cancer lesions (csPCa, PI-RADS  $\geq 4$ ), the Expert model. 2) Extract the PI-RADS scores from the radiology reports and count the number of csPCa lesions,  $n_{sig}$ . 3) Localise and segment the csPCa lesions, by keeping the  $n_{sig}$  most confident lesion candidates of the Expert Model. 4) Automatic annotations are used to augment the training dataset and train a new prostate cancer segmentation model.

Index lesion mark1: peripheral zone right apex.  
 T2W/DWI/DCE score: 4/4/+. Minimal ADC value: 821 (normally at least 950). Risk category: intermediate/high-grade cancer (PI-RADS v2 category: 4).

Score extraction → PI-RADS: 4, T2W: 4, DWI: 4, DCE: +

Finding nr. 1: peripheral zone right posterior mid-base prostate. Score T2W: 5, Score DCE: +, Score DWI: 5, minimal ADC value 665. Lesion best fits significant prostate cancer (PI-RADS 5).

Score extraction → PI-RADS: 5, T2W: 5, DWI: 5, DCE: +

**Fig. 2.** Example lesion report sections. The rule-based score extraction matched the T2W, DWI and DCE scores coloured orange, green and red, respectively. The resulting PI-RADS score is coloured purple. The reports were split in sections by matching the lesion identifier in blue. All reports were originally Dutch.

framework to zero-pad these scans, we extended the field of view slightly for this model, to 80.0 mm  $\times$  80.0 mm  $\times$  72.0 mm, which corresponds to a matrix size of 160  $\times$  160  $\times$  20.

*nnU-Net* comes with a predefined data preprocessing and augmentation pipeline, detailed in Supplementary Notes 2.2, 3.2 and 4 of (Isensee *et al.*, 2021). In short, T2W and DWI scans undergo instance-wise  $z$ -score normalisation, while ADC

maps undergo robust, global  $z$ -score normalisation with respect to the complete training dataset. For our anisotropic dataset, the *nnU-Net* framework applies affine transformations in 2D and applies a wide range of intensity and structure augmentations (Gaussian noise, Gaussian blur, brightness, contrast, simulation of low resolution and gamma augmentation).

For the *DA-UNet* model we used our institutional augmen-

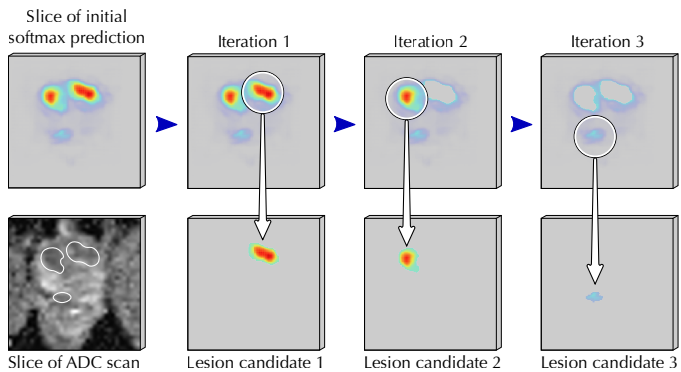


**Fig. 3. Depiction of the dynamic lesion candidate selection from a voxel-level prediction. The selected slice shows two high-confidence and one low-confidence lesion candidate extracted from the initial voxel-level prediction. All steps are performed in 3D.**

tation pipeline. We perform instance-wise min/max normalisation for T2W and DWI scans. For ADC maps, we divide each scan by 3000 (97.4<sup>th</sup> percentile), to retain their diagnostically relevant absolute values. Then, we apply Rician noise (Gudbjartsson and Patz, 1995) with  $\sigma = 0.01$  to each scan at original resolution, with a probability of 75%. Subsequently, we resample all scans to a uniform resolution of  $0.5 \text{ mm} \times 0.5 \text{ mm} \times 3.6 \text{ mm/voxel}$  with bicubic interpolation. Finally, with a probability of 50%, we apply 2D affine data augmentations: horizontal mirroring, rotation with  $\theta \sim 7.5 \cdot \mathcal{N}(0, 1)$ , horizontal translation with  $h_x \sim 0.05 \cdot \mathcal{N}(0, 1)$ , vertical translation with  $h_y \sim 0.05 \cdot \mathcal{N}(0, 1)$  and zoom with  $s_{xy} \sim 1.05 \cdot \mathcal{N}(0, 1)$ , where  $\mathcal{N}(0, 1)$  is a Gaussian distribution with zero mean and unit variance.

## 2.4. Experimental Analysis

### 2.4.1. Extraction of Report Findings

Accuracy of automatically counting the number of PI-RADS  $\geq 4$  lesions in a report ( $n_{\text{sig}}$ ) is determined by comparing against the number of PI-RADS  $\geq 4$  lesions in the manually annotated RUMC dataset. To account for multifocal lesions (which can be annotated as two distinct regions or a single larger one) and human error in the ground truth annotations, we manually checked the radiology report and verified the number of lesions when there was a mismatch between the ground truth and automatic estimation.

### 2.4.2. Localisation of Report Findings

Localisation of clinically significant report findings is evaluated with the sensitivity and average number of false positives per case. Evaluation is performed with 5-fold cross-validation on the labelled RUMC dataset, for which PI-RADS  $\geq 4$  lesions were manually annotated in the MRI scan.

### 2.4.3. Segmentation of Report Findings

Quality of the correctly localised report findings is evaluated with the Dice similarity coefficient (DSC). This evaluation is performed with 5-fold cross-validation on the labelled RUMC dataset, which has manual PI-RADS  $\geq 4$  lesion annotations.

### 2.4.4. Prostate Cancer Detection and Statistical Test

Prostate cancer detection models are evaluated on 300 external exams from ZGT, with histopathology-confirmed ground truth for all patients. Studies are considered positive if they have at least one Gleason grade group  $\geq 2$  lesion (csPCa) (Epstein et al., 2016). Patient-based diagnostic performance was evaluated using the Receiver Operating Characteristic (ROC), and summarised to the area under the ROC curve (AUROC). Lesion-based diagnostic performance was evaluated using Free-Response Receiver Operating Characteristic (FROC), and summarised to the partial area under the FROC curve (pAUC) between 0 and 1 false positive per case, similar to Saha et al. (2021). We trained our models with 5-fold cross-validation and 3 restarts for *nnU-Net* and 5 restarts for *DA-UNet*, resulting in 15 or 25 independent AUROCs and pAUCs on the test set for each model configuration. To determine the probability of one configuration outperforming another configuration, we performed a permutation test with 1,000,000 iterations. We used a statistical significance threshold of 0.01.

95% confidence intervals (CI) for the radiologists were determined by bootstrapping 1,000,000 iterations, with each iteration selecting  $\sim \mathcal{U}(0, N)$  samples with replacement and calculating the target metric. Iterations that sampled only one class were rejected.

### 2.4.5. Annotation-efficiency

Annotation-efficiency of semi-supervised training is defined as the fraction of manual annotations that are required to reach the same performance as with supervised training. With  $N_{\text{supervised}}$  the number of manually annotated exams used for supervised training and  $N_{\text{semi-supervised}}$  the number of manually annotated exams required to reach the same performance, we obtain the annotation-efficiency ratio:

$$R = \frac{N_{\text{supervised}}}{N_{\text{semi-supervised}}} \quad (1)$$

To construct a continuous curve for semi-supervised performance as function of the number of manually annotated exams, the performance of manual annotation budgets is piecewise logarithmically interpolated, as illustrated by the coloured dashed lines in the bottom row of Figure 6 (which appear linear with a logarithmic x-axis). The required number of manual annotations is then derived from the intersections, as illustrated by the black dashed lines in the bottom row of Figure 6. This evaluates to:

$$N_{\text{semi-supervised}} = N_a \cdot \left( \frac{N_b}{N_a} \right)^{\frac{(perf_{\text{supervised}} - perf_a)}{(perf_b - perf_a)}} \quad (2)$$

Where  $N_a$  is the number of manually annotated exams for the budget with performance just below supervised training,  $N_b$  is the number of manually annotated exams for the budget with performance just above supervised training,  $perf_{\text{supervised}}$  is the performance from supervised training,  $perf_a$  is the performance with semi-supervised training just below supervised training and  $perf_b$  is the performance with semi-supervised training just above supervised training.



Manual annotation budgets of 100, 300, 1,000 or 3,050 manually annotated exams, paired with the remaining 7,656, 7,456, 6,756 or 4,706 unlabelled exams were investigated. For supervised training with 5-fold cross validation, this corresponds to 80, 240, 800 or 2,440 manually annotated training samples per run. The supervised models are ensembled to generate automatic annotations for semi-supervised training, so for semi-supervised training the full manual annotation budgets are required.

### 3. Results

#### 3.1. Extraction of Report Findings

Our score extraction script correctly identified the number of clinically significant lesions for 3,024 out of the 3,044 (99.3%) radiology reports in our manually labelled RUMC dataset. We excluded reports and their studies when no PI-RADS scores could be extracted from the report: 8 cases (0.3%) from the labelled RUMC dataset and 121 cases (2.6%) from the unlabelled RUMC dataset. Full breakdown of automatically extracted versus manually determined number of significant lesions is given in Figure 4. Typing mistakes and changed scores in the addendum were the main source of the 20 (0.7%) incorrect extractions, which is an error rate similar to what we observed for our annotators.

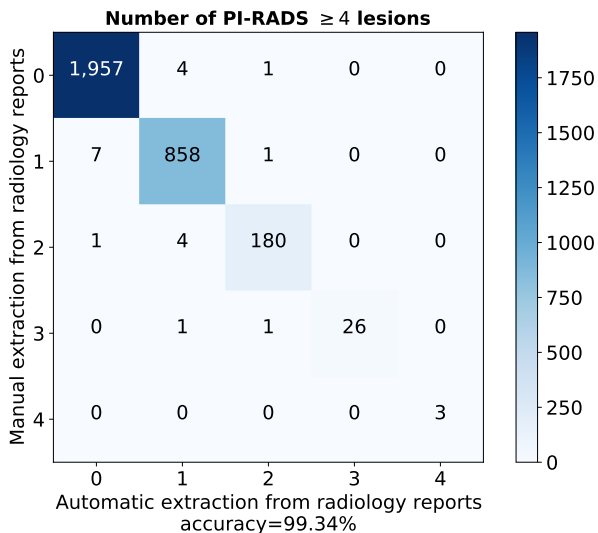


Fig. 4. Confusion matrix for number of clinically significant findings in a radiology report. Evaluated on the labelled RUMC subset.

#### 3.2. Localisation of Report Findings

Both prostate cancer segmentation architectures, *nnU-Net* and *DA-UNet*, can achieve high detection sensitivity. At this high sensitivity operating point, the models also propose a large number of false positive lesion candidates, as indicated by the Free-Response Receiver Operating Characteristic (FROC) curve shown in Figure 5. Masking the models' lesion candidates with the number of clinically significant report findings,  $n_{\text{sig}}$ , greatly reduces the number of false positive lesion candidates. At the sensitivity of the unfiltered automatic annotations,

masking with radiology reports reduced the average number of false positives per case from  $0.39 \pm 0.14$  to  $0.064 \pm 0.008$  for *nnU-Net* and from  $0.88 \pm 0.29$  to  $0.097 \pm 0.011$  for *DA-UNet* (trained with 5-fold cross-validation on 3,050 manually annotated exams). This more than five-fold reduction in false positives greatly increases the usability of the automatic annotations.

Studies where we could extract fewer than  $n_{\text{sig}}$  lesion candidates were excluded. This excludes studies where we are certain to miss lesions, and thus increases sensitivity. From the automatic annotations from *nnU-Net* we excluded 119 studies, resulting in a sensitivity of  $83.8 \pm 1.1\%$  at  $0.063 \pm 0.008$  false positives per study. From the automatic annotations from *DA-UNet* we excluded 4 studies, resulting in a sensitivity of  $78.5 \pm 3.3\%$  at  $0.096 \pm 0.012$  false positives per study.

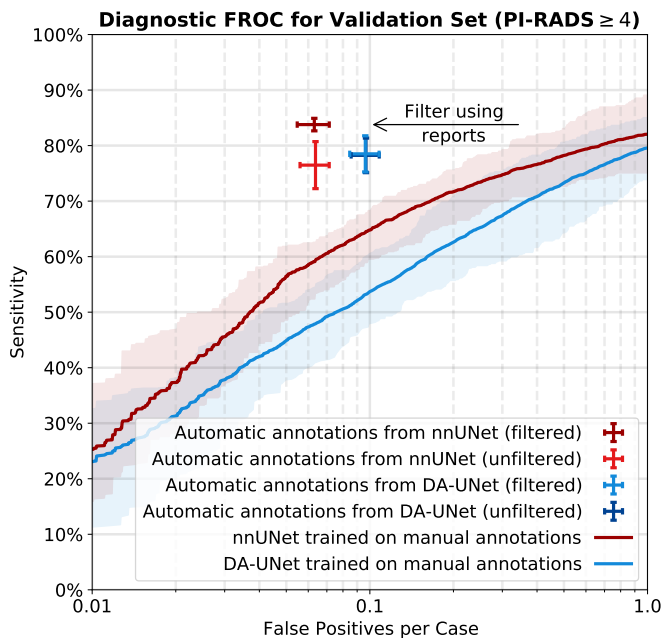


Fig. 5. Free-Response Receiver Operating Characteristic (FROC) curves for matching manually annotated PI-RADS  $\geq 4$  lesions. Shaded areas indicate the 95% confidence intervals. Masking model predictions with radiology reports significantly improves the false positive rate at high sensitivity, which is the useful range for annotations.

#### 3.3. Segmentation of Report Findings

Spatial similarity between the automatic and manual annotations is good. Trained with 5-fold cross-validation on 3,050 manual annotations, *nnU-Net* achieved a Dice similarity coefficient (DSC) of  $0.67 \pm 0.19$ , and *DA-UNet* achieved  $0.57 \pm 0.17$  DSC. Including the missed manual annotations as a DSC of zero, reduces this to  $0.51 \pm 0.33$  for *nnU-Net* and  $0.45 \pm 0.28$  for *DA-UNet*. The full distribution of DSC against lesion volume is given in the Supplementary Materials.

Figure 1 shows automatic annotations from *nnU-Net*, with a DSC of 0.70 ( $\approx$  mean) for the upper lesion of Patient 1, a DSC of 0.87 ( $\approx$  mean + std.) for Patient 2 and a DSC of 0.55 ( $\approx$  mean - std.) for Patient 3.

### 3.4. Prostate Cancer Detection

#### 3.4.1. Training with Report-guided Automatic Annotations

Semi-supervised training with 3,050 manually annotated and 4,706 automatically annotated exams significantly improved model performance, compared to supervised training with 3,050 manually annotated exams. For the external test set with histopathology-confirmed ground truth, the case-based AUROC increased from  $87.2 \pm 0.8\%$  to  $89.4 \pm 1.0\%$  ( $P < 10^{-4}$ ) for *nnU-Net* and from  $85.4 \pm 2.0\%$  to  $87.3 \pm 1.8\%$  ( $P = 4.0 \cdot 10^{-4}$ ) for *DA-UNet*.

On this external test set, a consensus of experienced radiologists had a sensitivity of  $93.2 \pm 2.7\%$  at  $75.9 \pm 2.9\%$  specificity. At the same sensitivity, adding automatically annotated exams improved the model's specificity from  $51.5 \pm 8.1\%$  to  $57.1 \pm 7.3\%$  ( $P = 0.28$ ) for *nnU-Net* and from  $35.8 \pm 11.3\%$  to  $46.7 \pm 11.8\%$  ( $P = 7.8 \cdot 10^{-3}$ ) for *DA-UNet*.

Detection and risk stratification of individual lesions also benefitted from including the automatically labelled training samples. Model performance, as measured by the pAUC, increased from  $0.692 \pm 0.030$  to  $0.746 \pm 0.016$  ( $P < 10^{-4}$ ) for *nnU-Net* and from  $0.697 \pm 0.034$  to  $0.727 \pm 0.038$  ( $P = 3.6 \cdot 10^{-3}$ ) for *DA-UNet*. Sensitivity at one false positive per case increased from  $76.4 \pm 3.8\%$  to  $83.6 \pm 2.3\%$  ( $P < 10^{-4}$ ) for *nnU-Net* and from  $77.7 \pm 4.0\%$  to  $81.3 \pm 3.9\%$  ( $P = 1.9 \cdot 10^{-3}$ ) for *DA-UNet*. See the top row of Figure 6 for the ROC and FROC curves.

#### 3.5. Annotation-efficiency of Training with Report-guided Automatic Annotations

Semi-supervised training significantly increased model performance for all investigated manual annotation budgets, compared to supervised training with the same number of manually annotated exams ( $P < 10^{-4}$  for each budget). Iteration 2 of semi-supervised training, where automatic annotations were generated by ensembling models from iteration 1 of semi-supervised training, generally performed better than iteration 1 of semi-supervised training. However, only AUROC improvement for manual annotation budgets of 100 and 300 exams were statistically significant ( $P = 3.9 \cdot 10^{-3}$  and  $P = 3.1 \cdot 10^{-3}$ ). ROC and FROC performances, summarised to the AUROC and pAUC, are shown in the bottom row of Figure 6.

Semi-supervised training (iteration 2) with 300 manual annotations exceeded case-based AUROC performance of supervised training with 2,440 manually annotated exams ( $P = 6.4 \cdot 10^{-3}$ ). Performance of semi-supervised training with 100 manually annotated exams came close ( $P = 0.014$ ). Interpolation suggests the supervised performance is matched with 169 manually annotated exams (14.4× more annotation-efficient).

Semi-supervised training (iteration 2) with 1,000 manually annotated exams exceeded lesion-based pAUC performance of supervised training with 2,440 manual annotations ( $P < 10^{-4}$ ). Performance of semi-supervised training with 300 manually annotated exams came close ( $P = 0.032$ ). Interpolation suggests the supervised performance is matched with 431 manually annotated exams (5.7× more annotation-efficient).

## 4. Discussion and Conclusion

Semi-supervised training significantly improved patient-based risk stratification and lesion-based detection performance of our prostate cancer detection models for all investigated manual annotation budgets, compared to supervised training with the same number of manually annotated exams. This improved performance demonstrates the feasibility of our semi-supervised training method with report-guided automatic annotations. Furthermore, the automatic annotations are of sufficient quality to speed up the manual annotation process, by identifying negative cases that do not need to be looked at, and by providing high quality segmentation masks for the majority of the positive cases. Our semi-supervised training method enabled us to utilise thousands of additional prostate MRI exams with radiology reports from clinical routine, without manually annotating each finding in the MRI scan.

Semi-supervised training with automatically labelled prostate MRI exams consistently improved model performance, with a group of baseline and augmented models truly reflecting the difference in performance due to the automatically labelled exams. Comparing groups of models ensures results are not due to variation in performance inherent to deep learning's stochastic nature<sup>2</sup>.

Automatically annotating training samples enables us to improve our models, but also speeds up the manual labelling process for new cases. Accurate PI-RADS score extraction from radiology reports enables us to automatically identify all negative cases (with  $\leq 1\%$  error rate), saving the repetitive operation of reading the radiology report only to designate a study as negative. As this entails approximately 60% of the studies, this already amounts to a large time saving. Furthermore, the segmentation masks from *nnU-Net* are often of sufficient quality to only require verification of the location, saving significant amounts of time for positive studies as well.

Direct applicability of the automatic PI-RADS extraction from radiology reports is, however, limited. The rule-based score extraction was developed with the report templates from RUMC in mind, and is likely to fail for reports with a different structure. For institutes that also have structured reports, the rule-based score extraction can be adapted to match their findings. For unstructured (free text) reports, the task of counting the number of clinically significant findings can be performed by a deep learning-based natural language processing model. This model can be trained on the reports of the manually labelled subset, using the number of findings found in the manual annotations as labels.

Another limitation is that the prostate cancer detection models were trained with prostate MRI scans from a single vendor (Siemens Healthineers, Erlangen; Magnetom Trio/Skyra/Prisma/Avanto). Therefore, these models are likely to perform inferior on scans from different scanner models.

In conclusion, semi-supervised training with report-guided automatic annotations significantly improved csPCa detection

<sup>2</sup>Sources of variation include the model's random initialisation, order of training batches and data augmentations, resulting in differences in model performance between training runs.

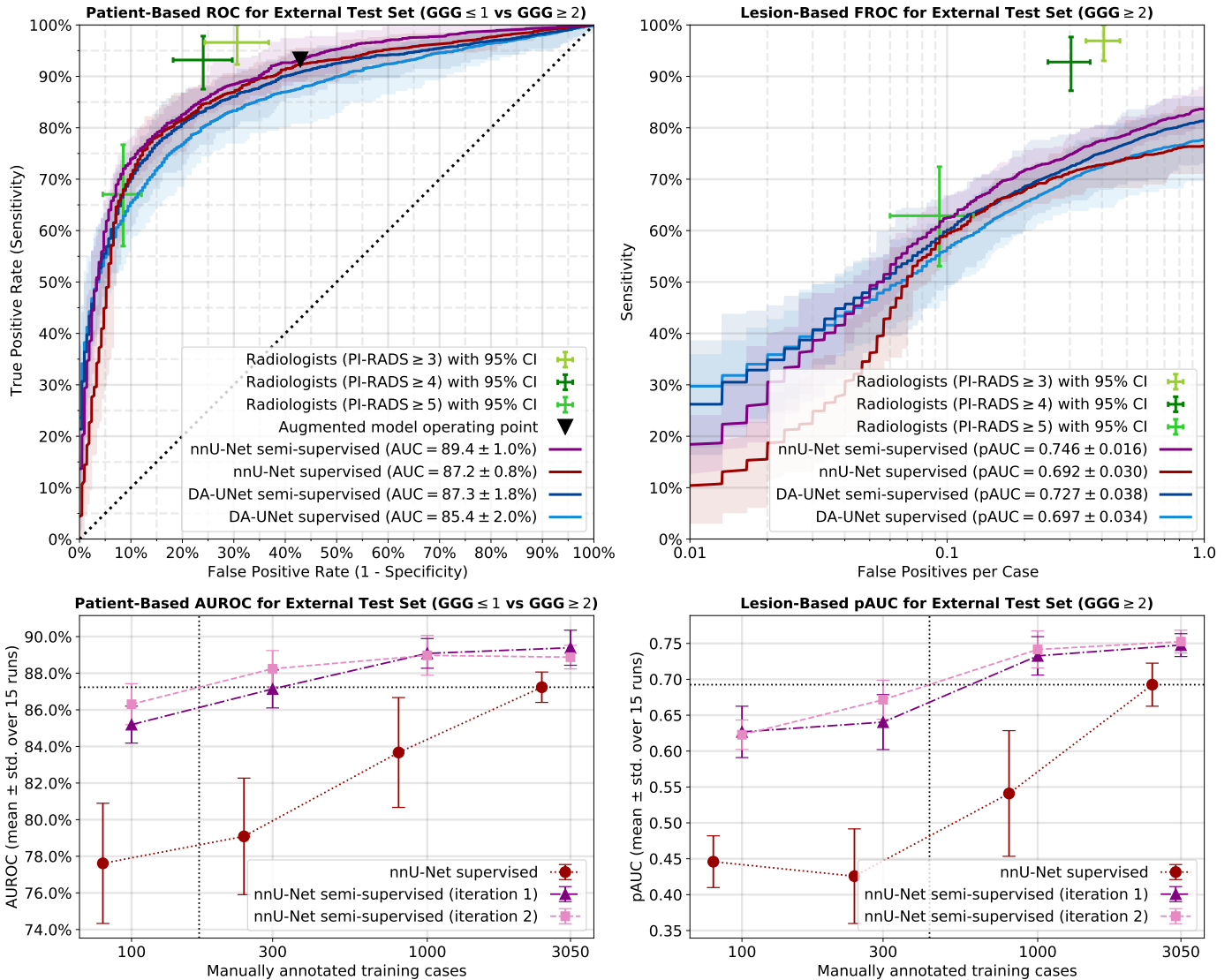


**Fig. 6.** (top row) Model performance for (semi)-supervised training. Supervised models are trained with 5-fold cross-validation on 3,050 manually annotated exams, and self-training also includes automatically annotated exams from 4,706 unlabelled exams. Automatic annotations for self-training are generated using the supervised models with the same architecture. (bottom row) *nnU-Net* performance for 100, 300, 1,000 or 3,050 manually annotated exams, combined with 7,656, 7,456, 6,756 or 4,706 unlabelled cases, respectively. Automatic annotations for iteration 1 are generated using the supervised models, automatic annotations for iteration 2 are generated using the semi-supervised models from iteration 1. The (left) panels show ROC performance for patient-based diagnosis of exams with at least one Gleason grade group (GGG)  $\geq$  2 lesion, and the (right) panels show FROC performance for lesion-based diagnosis of GGG  $\geq$  2 lesions. All models are trained on radiology based PI-RADS  $\geq$  4 annotations and evaluated on the external test set with histopathology-confirmed ground truth. Shaded areas indicate the 95% confidence intervals from 15 or 25 independent training runs.

performance, allowing unlabelled samples to be leveraged without additional manual effort. Furthermore, automatic annotations can speed up the manual annotation process. Our proposed method is widely applicable, paving the way towards larger datasets with equal or reduced annotation time.

## References

- Aldoj, N., Lukas, S., Dewey, M., Penzkofer, T., 2020. Semi-automatic classification of prostate cancer on multi-parametric MR imaging using a multi-channel 3D convolutional neural network. *European radiology* 30, 1243–1253.
- Ardila, D., Kiraly, A.P., Bharadwaj, S., Choi, B., Reicher, J.J., Peng, L., Tse, D., Etemadi, M., Ye, W., Corrado, G., et al., 2019. End-to-end lung cancer screening with three-dimensional deep learning on low-dose chest computed tomography. *Nature Medicine* 25, 954–961.
- Arif, M., Schoots, I.G., Tovar, J.C., Bangma, C.H., Krestin, G.P., Roobol, M.J., Niessen, W., Veenland, J.F., 2020. Clinically significant prostate cancer detection and segmentation in low-risk patients using a convolutional neural network on multi-parametric MRI. *European Radiology* 30, 6582–6592.
- Azizi, S., Mustafa, B., Ryan, F., Beaver, Z., Freyberg, J., Deaton, J., Loh, A., Karthikesalingam, A., Kornblith, S., Chen, T., et al., 2021. Big Self-Supervised Models Advance Medical Image Classification. *arXiv preprint arXiv:2101.05224*.
- Baumgartner, M., Jaeger, P.F., Isensee, F., Maier-Hein, K.H., 2021. nnDetection: A Self-configuring Method for Medical Object Detection. *arXiv preprint arXiv:2106.00817*.
- Bhattacharya, I., Seetharaman, A., Shao, W., Sood, R., Kunder, C.A., Fan, R.E., Soerensen, S.J.C., Wang, J.B., Ghanouni, P., Teslovich, N.C., et al., 2020. CorrSigNet: Learning CORRelated Prostate Cancer SIGNatures from Radiology and Pathology Images for Improved Computer Aided Diagnosis,



- in: International Conference on Medical Image Computing and Computer-Assisted Intervention, Springer. pp. 315–325.
- Bulten, W., Pinckaers, H., van Boven, H., Vink, R., de Bel, T., van Ginneken, B., van der Laak, J., de Kaa, C.H.v., Litjens, G., 2019. Automated Gleason Grading of Prostate Biopsies using Deep Learning. arXiv preprint arXiv:1907.07980 .
- Cao, R., Bajgiran, A.M., Mirak, S.A., Shakeri, S., Zhong, X., Enzmann, D., Raman, S., Sung, K., 2019. Joint Prostate Cancer Detection and Gleason Score Prediction in mp-MRI via FocalNet. *IEEE transactions on medical imaging* 38, 2496–2506.
- Cao, R., Zhong, X., Afshari, S., Felker, E., Suvannarerg, V., Tubtawee, T., Vangala, S., Scalzo, F., Raman, S., Sung, K., 2021. Performance of Deep Learning and Genitourinary Radiologists in Detection of Prostate Cancer Using 3-T Multiparametric Magnetic Resonance Imaging. *Journal of Magnetic Resonance Imaging* .
- Chaitanya, K., Erdil, E., Karani, N., Konukoglu, E., 2020. Contrastive learning of global and local features for medical image segmentation with limited annotations. arXiv preprint arXiv:2006.10511 .
- Cheplygina, V., de Bruijne, M., Pluim, J.P., 2019. Not-so-supervised: a survey of semi-supervised, multi-instance, and transfer learning in medical image analysis. *Medical Image Analysis* 54, 280–296.
- Çiçek, Ö., Abdulkadir, A., Lienkamp, S.S., Brox, T., Ronneberger, O., 2016. 3D U-Net: Learning Dense Volumetric Segmentation from Sparse Annotation, in: International Conference on Medical Image Computing and Computer-Assisted Intervention, Springer. pp. 424–432.
- Eldred-Evans, D., Burak, P., Connor, M.J., Day, E., Evans, M., Fiorentino, F., Gammon, M., Hosking-Jervis, F., Klimowska-Nassar, N., McGuire, W., et al., 2021. Population-Based Prostate Cancer Screening With Magnetic Resonance Imaging or Ultrasonography: The IP1-PROSTAGRAM Study. *JAMA Oncology* .
- Epstein, J.I., Egevad, L., Amin, M.B., Delahunt, B., Srigley, J.R., Humphrey, P.A., 2016. The 2014 International Society of Urological Pathology (ISUP) Consensus Conference on Gleason Grading of Prostatic Carcinoma. *The American Journal of Surgical Pathology* 40, 244–252.
- Gudbjartsson, H., Patz, S., 1995. The Rician distribution of noisy MRI data. *Magnetic Resonance in Medicine* 34, 910–914.
- Hosseinzadeh, M., Saha, A., Brand, P., Slootweg, I., de Rooij, M., Huisman, H., 2021. Deep learning–assisted prostate cancer detection on bi-parametric MRI: minimum training data size requirements and effect of prior knowledge. *European Radiology* , 1–11.
- Isensee, F., Jaeger, P.F., Kohl, S.A., Petersen, J., Maier-Hein, K.H., 2021. nnU-Net: a self-configuring method for deep learning-based biomedical image segmentation. *Nature Methods* 18, 203–211.
- Lin, T.Y., Goyal, P., Girshick, R., He, K., Dollár, P., 2017. Focal Loss for Dense Object Detection, in: Proceedings of the IEEE International Conference on Computer Vision, pp. 2980–2988.
- Liu, Y., Jain, A., Eng, C., Way, D.H., Lee, K., Bui, P., Kanada, K., de Oliveira Marinho, G., Gallegos, J., Gabriele, S., et al., 2020. A deep learning system for differential diagnosis of skin diseases. *Nature Medicine* 26, 900–908.
- Mahajan, D., Girshick, R., Ramanathan, V., He, K., Paluri, M., Li, Y., Bharambe, A., Van Der Maaten, L., 2018. Exploring the Limits of Weakly Supervised Pretraining, in: Proceedings of the European Conference on Computer Vision (ECCV), pp. 181–196.
- McKinney, S.M., Sieniek, M., Godbole, V., Godwin, J., Antropova, N., Ashrafiyan, H., Back, T., Chesus, M., Corrado, G.S., Darzi, A., et al., 2020. International evaluation of an AI system for breast cancer screening. *Nature* 577, 89–94.
- Netzer, N., Weißer, C., Schelb, P., Wang, X., Qin, X., Görtz, M., Schütz, V., Radtke, J.P., Hielscher, T., Schwab, C., Stenzinger, A., Kuder, T.A., Gnirs, R., Hohenfellner, M., Schlemmer, H.P., Maier-Hein, K.H., Bonekamp, D., 2021. Fully Automatic Deep Learning in Bi-institutional Prostate Magnetic Resonance Imaging: Effects of Cohort Size and Heterogeneity. *Investigative radiology* .
- Pham, H., Dai, Z., Xie, Q., Le, Q.V., 2021. Meta Pseudo Labels, in: Proceedings of the IEEE/CVF Conference on Computer Vision and Pattern Recognition (CVPR), pp. 11557–11568.
- Ronneberger, O., Fischer, P., Brox, T., 2015. U-Net: Convolutional Networks for Biomedical Image Segmentation, in: International Conference on Medical image computing and computer-assisted intervention, Springer. pp. 234–241.
- Saha, A., Hosseinzadeh, M., Huisman, H., 2021. End-to-end Prostate Cancer Detection in bpMRI via 3D CNNs: Effects of Attention Mechanisms, Clinical Priori and Decoupled False Positive Reduction. *Medical Image Analysis* , 102155.
- Sanford, T., Harmon, S.A., Turkbey, E.B., Kesani, D., Tuncer, S., Madariaga, M., Yang, C., Sackett, J., Mehravivand, S., Yan, P., et al., 2020. Deep-Learning-Based Artificial Intelligence for PI-RADS Classification to Assist Multiparametric Prostate MRI Interpretation: A Development Study. *Journal of Magnetic Resonance Imaging* 52, 1499–1507.
- Sanyal, J., Banerjee, I., Hahn, L., Rubin, D., 2020. An Automated Two-step Pipeline for Aggressive Prostate Lesion Detection from Multi-parametric MR Sequence. *AMIA Summits on Translational Science Proceedings 2020*, 552.
- Schelb, P., Kohl, S., Radtke, J.P., Wiesenfarth, M., Kickingereider, P., Bickelhaupt, S., Kuder, T.A., Stenzinger, A., Hohenfellner, M., Schlemmer, H.P., et al., 2019. Classification of Cancer at Prostate MRI: Deep Learning versus Clinical PI-RADS Assessment. *Radiology* 293, 607–617.
- Seetharaman, A., Bhattacharya, I., Chen, L.C., Kunder, C.A., Shao, W., Soerensen, S.J., Wang, J.B., Teslovich, N.C., Fan, R.E., Ghanouni, P., et al., 2021. Automated detection of aggressive and indolent prostate cancer on magnetic resonance imaging. *Medical Physics* .
- Sowrirajan, H., Yang, J., Ng, A.Y., Rajpurkar, P., 2021. MoCo pretraining improves representation and transferability of chest X-ray models, in: *Medical Imaging with Deep Learning*, PMLR. pp. 728–744.
- Stavriniades, V., Giganti, F., Emberton, M., Moore, C.M., 2019. MRI in active surveillance: a critical review. *Prostate Cancer and Prostatic Diseases* 22, 5–15.
- Sung, H., Ferlay, J., Siegel, R.L., Laversanne, M., Soerjomataram, I., Jemal, A., Bray, F., 2021. Global Cancer Statistics 2020: GLOBOCAN Estimates of Incidence and Mortality Worldwide for 36 Cancers in 185 Countries. *CA: A Cancer Journal for Clinicians* 71, 209–249.
- Xie, Q., Luong, M.T., Hovy, E., Le, Q.V., 2020. Self-Training With Noisy Student Improves ImageNet Classification, in: Proceedings of the IEEE/CVF Conference on Computer Vision and Pattern Recognition, pp. 10687–10698.
- Yu, X., Lou, B., Shi, B., Winkel, D., Arrahmane, N., Diallo, M., Meng, T., von Busch, H., Grimm, R., Kiefer, B., et al., 2020a. False Positive Reduction Using Multiscale Contextual Features for Prostate Cancer Detection in Multi-Parametric MRI Scans, in: 2020 IEEE 17th International Symposium on Biomedical Imaging (ISBI), IEEE. pp. 1355–1359.
- Yu, X., Lou, B., Zhang, D., Winkel, D., Arrahmane, N., Diallo, M., Meng, T., von Busch, H., Grimm, R., Kiefer, B., et al., 2020b. Deep Attentive Panoptic Model for Prostate Cancer Detection Using Biparametric MRI Scans, in: International Conference on Medical Image Computing and Computer-Assisted Intervention, Springer. pp. 594–604.
- Zhou, Z., Sodha, V., Siddiquee, M.M.R., Feng, R., Tajbakhsh, N., Gotway, M.B., Liang, J., 2019. Models Genesis: Generic Autodidactic Models for 3D Medical Image Analysis, in: International conference on medical image computing and computer-assisted intervention, Springer. pp. 384–393.

## Supplementary Materials

### A. Study Population

*Table A.* Patient demographic and characteristics for datasets acquired at Radboud University Medical Centre (RUMC) and Ziekenhuisgroep Twente (ZGT). Characteristic values are followed by their interquartile range (IQR), if applicable.

Characteristic	RUMC	ZGT
Number of Patients	6,380	300
Number of Studies	7,756	300
• Benign	4,734 <sup>§</sup>	212
• Malignant ( $\geq 1$ csPCa*)	3,022 <sup>§</sup>	88
Median PSA (ng/mL)	8.0 (5 – 11)	6.6 (5 – 9)
Median Age (years)	66 (61 – 70)	65 (59 – 68)
Median Prostate Volume (cm <sup>3</sup> )	64 (46 – 91)	50 (40 – 69)
MRI Scanners (3 T, Surface Coils)		
• Magnetom Trio/Skyra <sup>+</sup>	88.9%	100%
• Magnetom Prisma <sup>+</sup>	11.0%	–
• Magnetom Avanto <sup>+</sup> (1.5 T)	0.1%	–
T2W Acquisition		
• In-Plane Resolution (mm/voxel)	0.30 $\pm$ 0.08	0.50 $\pm$ 0.00
• Slice Thickness (mm/voxel)	3.60 $\pm$ 0.20	3.00 $\pm$ 0.00
DWI/ADC Acquisition		
• In-Plane Resolution (mm/voxel)	2.00 $\pm$ 0.05	2.00 $\pm$ 0.00
• Slice Thickness (mm/voxel)	3.60 $\pm$ 0.20	3.00 $\pm$ 0.00
• Computed High b-Value	b1400	b1400
MRI-Detected Lesions		
• PI-RADS $\leq 2$	5,958 <sup>§</sup>	248
• PI-RADS 3	983 <sup>§</sup>	35
• PI-RADS 4	2,115 <sup>§</sup>	92
• PI-RADS 5	1,508 <sup>§</sup>	89
Histopathology-Confirmed Lesions		
• GGG 1 (GS $\leq 3 + 3$ )	N/A	94
• GGG 2 (GS 3 + 4)	N/A	63
• GGG 3 (GS 4 + 3)	N/A	11
• GGG 4 (GS 4 + 4)	N/A	5
• GGG 5 (GS $\geq 4 + 5$ )	N/A	18

\* RUMC csPCa: PI-RADS  $\geq 4$ ; ZGT csPCa: GGG  $\geq 2$

<sup>+</sup> Siemens Healthineers, Erlangen, Germany

<sup>§</sup> Determined semi-automatically

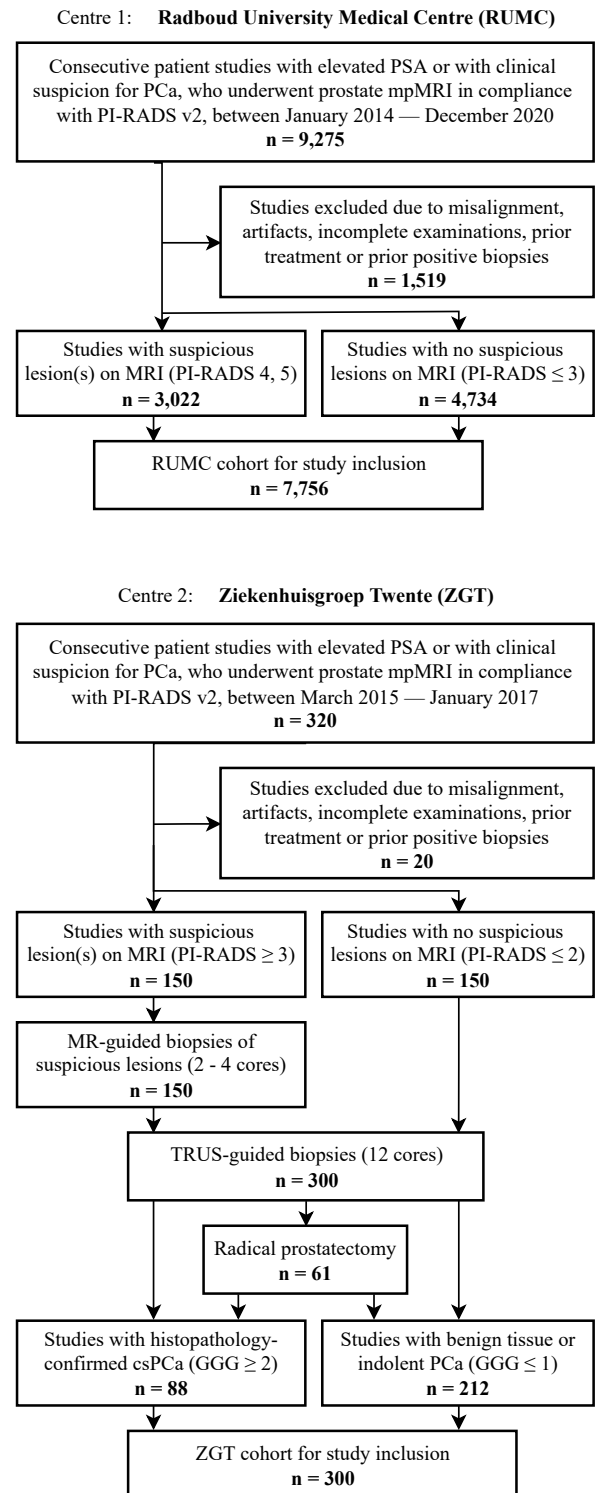


**Fig. A.** STARD diagram for study inclusion/exclusion criteria applied across both centres: Radboud University Medical Centre (RUMC) and Ziekenhuisgroep Twente (ZGT).

## B. Extraction of Report Findings

First, we tried to split the radiology reports in sections for individual findings, by searching for text that matches the following structure:

[Finding] (number indicator) [number]

Where ‘Finding’ matches the Dutch translations ‘*afwijking*’, ‘*laesie*’, ‘*markering*’ or ‘*regio*’. The optional number indicators are ‘*nr.*’, ‘*mark*’ and ‘*nummer*’. The number at the end matches one or multiple numbers (e.g., ‘1’ or ‘2+3’).

Secondly, we extracted the PI-RADS scores by searching for text that matches the following structure:

[PI-RADS] (separators) [number 1-5]

Where the optional separators include ‘*v2 category*’ and ‘*:*’. The dash between ‘*PI*’ and ‘*RADS*’ is optional. The T2W, DWI and DCE scores, which define the PI-RADS score, are extracted analogous to the PI-RADS score, while also allowing joint extraction:

T2W/DWI/DCE score: [1-5] / [1-5] / [-+]

In this instance, the first number is matched with the T2W score, the second with DWI and the + or - with DCE.

In case the report could not be split in sections per lesion, we applied strict pattern matching on the full report. During strict pattern matching we only extract T2W, DWI and DCE scores jointly, to ensure the scores are from the same lesion. The resulting PI-RADS scores were extracted from the full report and matched to the individual scores.

## C. Detection Model Architecture

For our prostate cancer segmentation task, *nnU-Net* [1] configured itself to use a 3D *U-Net* with five down-sampling steps, as shown in Figure B. This figure also shows the specific choice of 2D/3D convolutional blocks, max-pooling layers and transposed convolutions. No cascade of *U-Nets* or 2D *U-Net* was triggered for our dataset.

The implementation of the *DA-U-Net* architecture is the same as in [2], with the exception of *LeakyReLU* [3] activation functions throughout the decoder and decreased  $L_2$  kernel regularisation of  $10^{-4}$ . See [2] for implementation details.

- [1] F. Isensee, P. F. Jaeger, S. A. Kohl, J. Petersen, and K. H. Maier-Hein, “nnU-Net: a self-configuring method for deep learning-based biomedical image segmentation,” *Nature Methods*, vol. 18, no. 2, pp. 203–211, 2021.
- [2] A. Saha, M. Hosseinzadeh, and H. Huisman, “End-to-end Prostate Cancer Detection in bpMRI via 3D CNNs: Effects of Attention Mechanisms, Clinical Priori and Decoupled False Positive Reduction”, *Medical Image Analysis*, p. 102 155, 2021, ISSN: 1361-8415.
- [3] A. L. Maas, A. Y. Hannun, and A. Y. Ng, “Rectifier Non-linearities Improve Neural Network Acoustic Models”, in *Proc. icml, Citeseer*, vol. 30, 2013, p. 3.

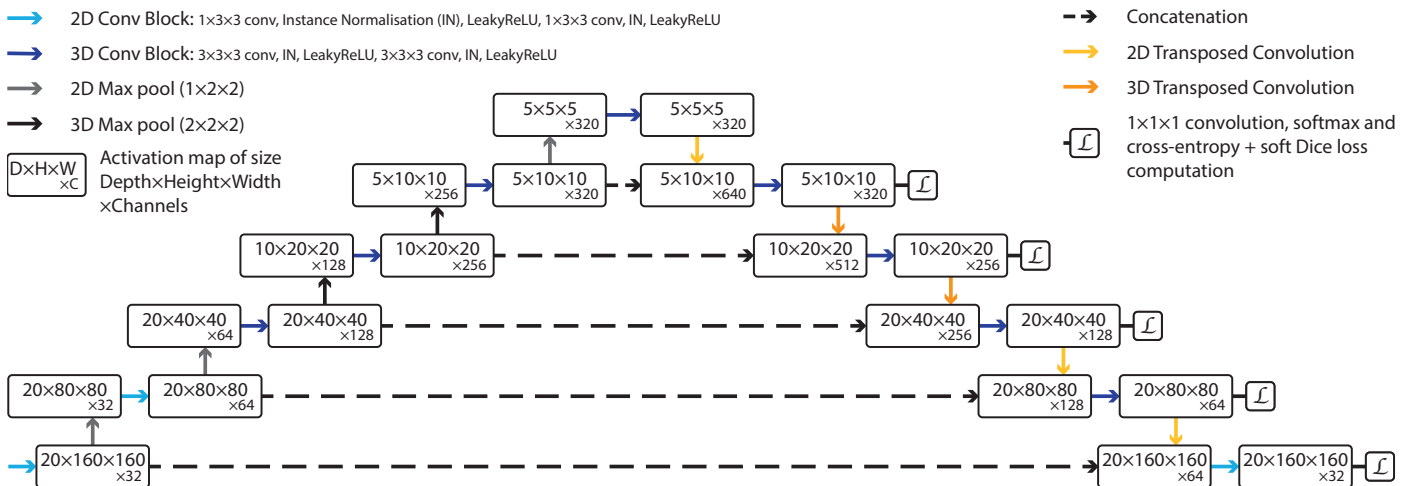
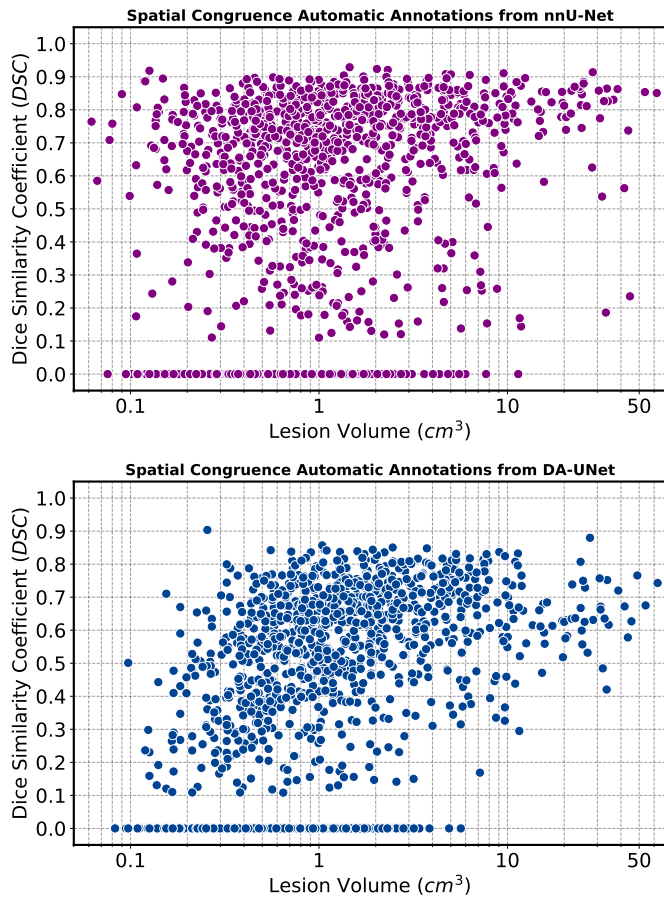


Fig. B. Architecture schematic of the *nnU-Net*, as configured for our prostate cancer segmentation task.

## D. Lesion Segmentation Quality



**Fig. C.** Spatial congruence between automatic and manual csPCa annotations, as measured by the Dice similarity coefficient, for automatic annotations derived from (top) *nnU-Net* or (bottom) *DA-UNet*. Both methods were evaluated on the labelled RUMC dataset with 5-fold cross-validation, excluded studies due to empty PI-RADS extraction from the radiology report, and excluded studies with insufficient lesion candidates. All metrics were computed in 3D.